Analysis and Low-order Modeling of the Three-dimensional Flow Past a Confined Square Cylinder

Marcelo Buffoni, Simone Camarri, Angelo Iollo, Maria-Vittoria Salvetti

INSTITUT NATIONAL DE RECHERCHE EN INFORMATIQUE ET EN AUTOMATIQUE

Analysis and Low-order Modeling of the Three-dimensional Flow Past a Confined Square Cylinder

Marcelo Buffoni — Simone Camarri — Angelo Iollo — Maria Vittoria Salvetti

N° 6004

Octobre 2006

Thème NUM

ISSN 0249-6399

Analysis and Low-order Modeling of the Three-dimensional Flow Past a Confined Square Cylinder

Marcelo Buffoni[*†] , Simone Camarri[‡] , Angelo Iollo[†] , Maria Vittoria Salvetti[‡]

Thème NUM — Systèmes numériques
Projet MC2

Rapport de recherche n° 6004 — Octobre 2006 — 18 pages

Abstract: The laminar flow past a square cylinder symmetrically placed between two parallel walls is considered. A classical vortex wake is shed from the cylinder, but three-dimensional instabilities are present and they develop in complicated flow patterns. The possibility of extracting an accurate low-order model of this flow is explored.

Key-words: low-order models, wake flows, proper orthogonal decomposition

[*] DIASP - Politecnico di Torino, 10129 Torino, Italy
[†] MAB - Université Bordeaux 1 et MC2 - INRIA Futurs, 33405 Talence, France
[‡] DIA - Università di Pisa, 56127 Pisa,Italy

Unité de recherche INRIA Futurs
Parc Club Orsay Université, ZAC des Vignes,

Analyse et modèle d'ordre réduit d'un écoulement tridimensionnel autour d'un cylindre carré confiné

Résumé : Nous considérons un écoulement laminaire autour d'un cylindre carré placé de façon symétrique entre deux parois parallèles. Un sillage tourbillionnaire classique se crée derrière le cylindre, mais des instabilités tridimensionnelles sont présentes et se développent suivant des motifs compliqués. Nous explorons la possibilité d'extraire un modèle d'ordre réduit fiable de cet écoulement.

Mots-clés : modèles réduits, écoulement de sillage, décomposition orthogonale aux valeurs propres

1 Introduction

Since the introduction in fluid mechanics of model reduction ideas ([9]), one of the main concerns is to use small dimensional surrogates to replace the actual Navier-Stokes equations for control purposes. One application often targeted is the control of vortex shedding ([7]); the benefits of such technology would range from reduced fatigue on materials and lower noise emissions, to flight of thick-wing airships. Even though examples of vortex shedding control built on low-order models and solid optimisation grounds recently appeared ([1]), they are limited to two-dimensional laminar flows. One of the reasons is that low order models based on straight forward Galerkin projection over empirical eigenmodes and *ad hoc* additional dissipation, fail to represent the correct dynamics as soon as it is not a simple oscillation. Also it is not clear whether a low dimensional representation of more complex flows can be found, and in fact there are examples where such a representation does not exist ([18]).

In this contribution two issues are investigated: the possibility (i) of giving a small dimensional representation of a fairly complicated flow and (ii) of deriving an accurate dynamical model from such a representation. In this respect [11], [6] and [5] addressed similar questions for simpler flows. Here we try to advance in flow complexity and in the related numerical technology, based on the pseudo-spectral calibration approach introduced in [5].

To this end, we concentrate on the case of a square cylinder placed at midspan between two parallel flat walls. The Reynolds numbers considered are such that the flow is characterised by a three-dimensional vortex wake that interferes with the upper and lower walls.

The first part of this paper is dedicated to a description of the numerical set-up as well as to an interpretation of the results obtained. Next, low order models of the impulsive start-up as well as of the developed flow regime are investigated.

2 Numerical simulation

The adopted configuration is sketched in figure 1. The ratio between the cylinder side L and the distance between the walls H is $L/H = 1/8$. The incoming flow is a laminar Poiseuille flow directed in the x direction and the considered Reynolds numbers, based on the maximum velocity of the incoming flow and on L, range between 100 and 300. The Navier-Stokes equations for compressible flows were discretized in space using a mixed finite-volume/finite-element method applied to unstructured tetrahedrizations. The adopted scheme is vertex centered and P1 Galerkin finite elements are used to discretize the diffusive terms.

A dual finite-volume grid is obtained by building a cell C_i around each vertex i through the rule of medians. The convective fluxes are discretized on this tessellation, i.e. in terms of fluxes through the common boundaries shared by neighboring cells.

The Roe scheme ([14]) represents the basic upwind component for the numerical evaluation of the convective fluxes $\mathcal{F}$:

$$\Phi^R\left(W_i,\, W_j,\, \vec{n}\right) = \frac{\mathcal{F}\left(W_i,\, \vec{n}\right) + \mathcal{F}\left(W_j,\, \vec{n}\right)}{2} - \gamma_s P^{-1} |P\mathcal{R}| \, \frac{\left(W_j - W_i\right)}{2}$$

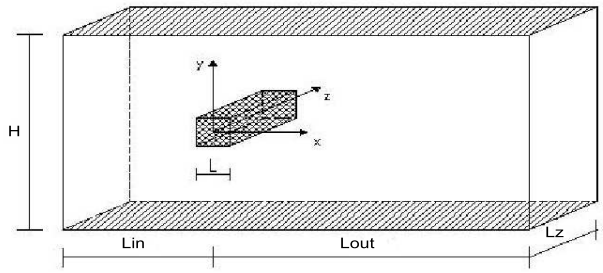

Figure 1: Computational domain

in which, $\Phi^R\left(W_i,\ W_j,\ \vec{n}\right)$ is the numerical approximation of the flux between the i-th and the j-th cells, W_i is the solution vector at the i-th node, $\vec{n}$ is the outward normal to the cell boundary and $\mathcal{R}\left(W_i,\ W_j,\ \vec{n}\right)$ is the Roe matrix. The matrix $P(W_i,\ W_j)$ is the Turkel-type preconditioning term, introduced to avoid accuracy problems at low Mach numbers ([8]). Finally, the parameter γ_s, which multiplies the upwind part of the scheme, permits a direct control of the numerical viscosity, leading to a full upwind scheme for $\gamma_s = 1$ and to a centered scheme when $\gamma_s = 0$. The spatial accuracy of this scheme is only first order. The MUSCL linear reconstruction method ("Monotone Upwind Schemes for Conservation Laws"), introduced by [19], is employed to increase the order of accuracy of the Roe scheme. This is obtained by expressing the Roe flux as a function of the reconstructed values of W at the cell interface: $\Phi^R\left(W_{ij},\ W_{ji},\ \vec{n}_{ij}\right)$, where W_{ij} is extrapolated from the values of W at nodes i and j. A reconstruction using a combination of different families of approximate gradients (P1-elementwise gradients and nodal gradients evaluated on different tetrahedra) is adopted, which allows a numerical dissipation made of sixth-order space derivatives to be obtained. The MUSCL reconstruction is described in detail in [4], in which the capabilities of this scheme in concentrating the numerical viscosity effect on a narrow-band of high-frequency fluctuations is also discussed.

The time marching algorithm is implicit and based on a backward difference scheme. A first-order semi-discretization of the jacobians is adopted together with a defect-correction procedure ([12]); the resulting scheme is second-order accurate in time.

The method of characteristics is used to impose non-reflective inflow and outflow boundary conditions. At the inflow the Poiseuille flow is assumed to be undisturbed. Periodic boundary conditions are imposed in the spanwise direction and no-slip conditions are forced on the cylinder and on the parallel walls.

Two different computational domains were used, for carrying out two-dimensional and three-dimensional simulations, which differ only for the spanwise extent of the domain. In both cases, with reference to figure 1, $L_{in}/L = 12$ and $L_{out}/L = 20$. For two-dimensional simulations, the spanwise length adopted is $L_z/L = 0.6$, and it was systematically checked that the simulated spanwise velocity was negligible. For the three-dimensional simulations, the spanwise length of the domain is $L_z/L = 6$. This value was selected following the experimental results for the unconfined square-cylinder flow ([10]), which show a maximum spanwise length of the three-dimensional

structures equal to $5.2L$ and the indications given in [17] and [15] for the numerical study of the three-dimensional wake instabilities of a square cylinder in an open uniform flow.

Grid convergence tests were carried out in the two-dimensional simulations using three grids, mainly differing for the spatial resolution in the proximity of the cylinder. Details of the grids are reported in table 1. The grid GR4, used for the three-dimensional simulations, was built by replicating grid GR1 10 times in the spanwise direction (see table 1). Since we intend to simulate an

grid	total number of nodes	nodes on the cylinder perimeter	L_z/L
GR1	$7.5 \cdot 10^5$	250	0.6
GR2	$6.6 \cdot 10^5$	210	0.6
GR3	$6.0 \cdot 10^5$	170	0.6
GR4	$6.6 \cdot 10^6$	250	6.0

Table 1: Details of the grids used in the simulations

incompressible flow, the simulations were performed by assuming that the maximum Mach number of the inflow profile is $M = 0.1$. This value allows compressibility effects to be reasonably neglected in the results. The preconditioning described above is used to increase the accuracy of the results. It was observe during preliminary simulations that the preconditioner led to a more accurate value of the pressure coefficient near the stagnation points in the upwind cylinder face, improving the mean value of the drag coefficient. The time fluctuations of the force coefficients were insensitive to the preconditioner. Concerning the numerical viscosity, the upwind parameter γ was set to $\gamma = 1.0$ on the nodes within a distance equal to $0.1L$ from the cylinder and $\gamma = 0.1$ in the rest of the domain. This choice ensured the stability of all the simulations carried out and, at the same time, allowed the preconditioner to be particularly effective in the proximity of the cylinder.

In order to validate the numerical approach and to perform a grid convergence study, two-dimensional numerical simulations were carried out for $Re = 100, 180$ and 300, on grids GR1, GR2 and GR3. The results were compared with those obtained for the same configuration in [2] and in [6], with different numerical methods and grid resolutions. The main bulk parameters characterizing the aerodynamics forces acting on the cylinder are shown in table 2; as can be seen the agreement with the results obtained in the literature is satisfactory. Moreover, it may be concluded that grid independence was almost reached, since in all cases the difference between the parameter values obtained with the different grids is very low ($\leq$ 2%, except for A_{CD}, which is, however, almost negligible in most cases). Note that for the Strouhal number, the scatter between our results is lower than that between the data in the literature. As an example of the vorticity fields typical of these 2D simulations, figure 3 shows the instantaneous vorticity isocontours obtained in the simulation at $Re = 180$ on grid GR1. The strong interaction with the confining walls adds to the complexity of the flow and leads to some peculiar features, like the fact that the vertical position of the spanwise vortices is opposite to the one in the classical von Kármán's street. Indeed, as it can be seen in the instantaneous vorticity isocontours obtained for $Re = 180$ on GR1 (see figure 3), clockwise vortices shed from the upper edge of the cylinder are located lower in the street than the counterclockwise

	Re	St	$\overline{C}_D$	A_{C_D}	A_{C_L}
GR1	300	0.1250	1.6205	0.4889	3.4019
GR2	300	0.1234	1.6359	0.5151	3.4635
GR3	300	0.1237	1.6509	0.5191	3.4807
Breuer et al.	300	0.1271	1.8603	0.5081	3.3534
Galletti et al.	300	0.1320	—	—	—
GR1	180	0.1404	1.3659	0.0463	0.9303
GR3	180	0.1388	1.3803	0.0459	0.9423
Breuer et al.	180	0.1440	1.3250	0.0490	0.9090
Galletti et al.	180	0.1370	—	—	—
GR1	100	0.1368	1.3758	0.0065	0.3715
GR3	100	0.1362	1.3820	0.0066	0.3638
Breuer et al.	100	0.1391	1.3500	0.0077	0.3835
Galletti et al.	100	0.1386	—	—	—
GR4(3D)	300	0.1345	1.4596	0.0876	1.1889

Table 2: Main bulk coefficients characterizing the aerodynamics forces acting on the cylinder and details of the grids used. St is the shedding frequency, $\overline{C}_D$ is the time averaged drag coefficient, A_{C_D} and A_{C_L} are the maximum amplitude of the oscillations of the drag and lift coefficients respectively. All previous quantities are made non-dimensional by using L and the maximum velocity of the incoming flow.

ones. This particular phenomenon, investigated by [3], was also observed in [6], and for a confined circular cylinder in [20].

Although this peculiar structure of the vortex street, at $Re = 100$ and 180 the behavior of the aerodynamic forces is the one typically found in 2D simulations of bluff body flows as shown in figure 2 for $Re = 180$. The time variation of the lift coefficient is perfectly periodic at the shedding frequency, while the C_D also exhibits a perfectly periodic oscillation at the harmonic frequency (not shown here for sake of brevity). At $Re = 300$ (see figure 2) the lift coefficient still shows periodic oscillations in time but with an amplitude modulation having a period of approximately three shedding cycles. A similar behavior, which is absent in 3D simulations, has been observed in other 2D simulations at the same Reynolds number of the flow around unconfined ([17]) and confined (C.-H. Bruneau, private communication) square cylinders, and might be interpreted as a signal of the unsuitability of 2D simulations for this Reynolds number.

Three-dimensional simulations were carried on grid GR4 at $Re = 200$ and 300. The simulations are initiated from an impulsive start-up and the transient phase was recorded and analyzed in order to investigate the mechanisms of formation of three-dimensional structures.

In figures. 4(a) and 4(b) the time behavior of the lift coefficient is shown for $Re = 200$ and $Re = 300$ respectively. The values of the maximum and minimum spanwise velocity in the field are also reported as an indicator of the occurrence of three-dimensional phenomena in the flow. As it can be seen, at $Re = 200$ an almost two-dimensional vortex shedding takes place at first, characterized by large amplitude oscillations ($60 < t < 120$). Three-dimensional phenomena grow more slowly and

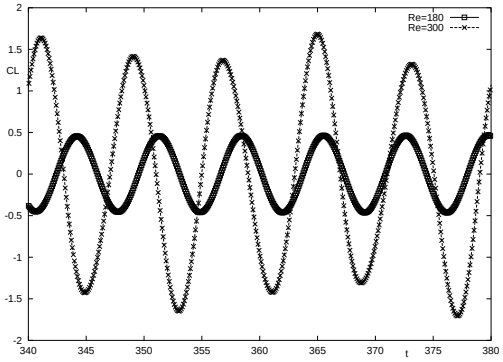

Figure 2: Time variation of the lift coefficient in 2D simulations at Re=180 and Re=300 on grid GR1

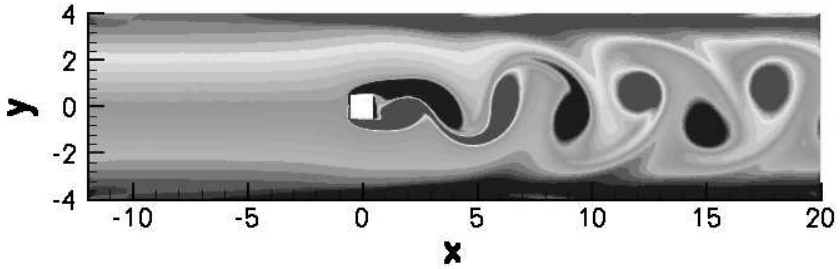

Figure 3: Instantaneous vorticity obtained in the 2D simulation at $Re = 180$ on GR1.

their effects on the aerodynamic forces become visible only for $t > 120$, with a significant reduction of the oscillation amplitude of C_L and of the mean value of the drag coefficient (see table 2), due to the loss of coherence of the vortex shedding in the spanwise direction. Conversely, at $Re = 300$, as expected, the three-dimensional instabilities grow more rapidly and three-dimensional effects on the aerodynamic forces are already significant when the vortex shedding phenomenon begins to take place. Let us now analyze in more detail the form of the three-dimensional instabilities and structures. Two different instability modes, initially identified in circular cylinder flows, were also found for unconfined square cylinders in experiments ([10]) and in the Floquet instability analysis ([13]). The first one, mode A, occurs at lower Re and is characterized by the formation of large scale and wavy vortex loops that connect the spanwise von Kármán vortices. The second one, mode B, is characterized by shorter, finer scaled vortex loops. For unconfined square cylinders, mode A was found to occur at $Re \simeq 160$ with a spanwise wavelength of $5.2L$, while mode B at $Re = 190 \div 200$ with a spanwise wavelength of $1.2L$. A third instability mode having a spanwise wavelength of $2.8L$ (mode S) was also identified through the Floquet analysis, which was not, however, observed in the experiments. In order to visualize the vortex loops typical of three-dimensional instability, in figure 5(a) two isosurfaces of the streamwise vorticity, obtained in the simulation at $Re = 200$, are shown

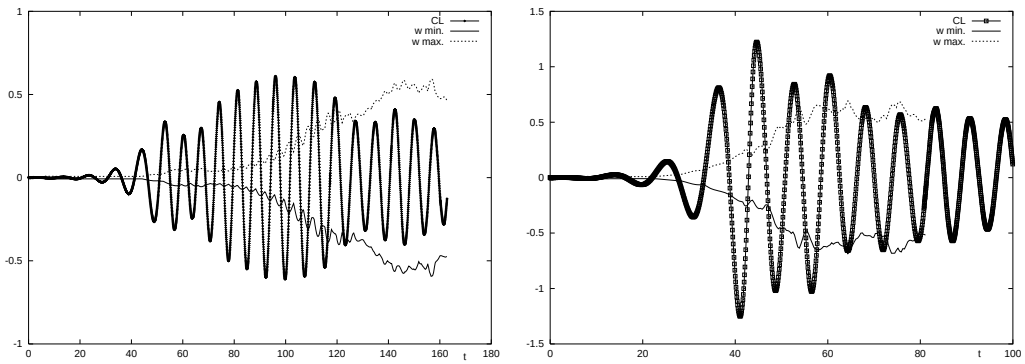

(a) (b)

Figure 4: Time variation of the lift coefficient and of the maximum and minimum of the spanwise velocity obtained in the three-dimensional simulation at (a) $Re = 200$; (b) $Re = 300$.

at a time, during the transient, for which the spanwise velocity reached approximately 10% of the maximum inflow velocity. The structures in figure 5(a) are those typical of mode A of instability (see, for instance, the visualizations in [13]). However, in our case these structures have a spanwise wave length of approximately 6D due to the imposed periodicity in the spanwise direction. The predominance of mode A is maintained also at the latest stages of the transient available at present in our simulation; thus, it is plausible to conclude that at this Re three-dimensional transition still follows mode A, while for unconfined cylinders the onset of mode B was found at $Re = 190 \div 200$. At $Re = 300$, since the early stages of transition, the situation is more complex, as shown in figure 5(b), in which two isosurfaces of the streamwise vorticity are reported at a time at which the spanwise velocity reached approximately 10% of the maximum inflow velocity. Indeed, mode-A-type structures tend to break in smaller vortical loops, not yet showing however a well defined spanwise length. Later on in the transient (figure 6(a)), only these smaller structures are practically visible, which have now a much better defined periodical behavior with a spanwise wave-length of approximately $1L$ and are, thus, very likely related with the instability mode B. These structures persist after the end of the transient (see figure 6(b)) and in the developed three-dimensional wake they connect the vortex tubes of the von Kármán street (in black and light gray in figure 6(b)). These spanwise vortex tubes are in turn corrugated and distorted by the motion induced by the streamwise vortices. Figure 7 shows the isocontours of the modulus of the projection of vorticity on a (y, z) plane in the wake together with the velocity vectors (v and w components) on the same plane. Indeed, the shear layer is clearly deformed by the vortical motion induced by the streamwise vortex loops and this is a typical scenario of three-dimensional wakes at moderate Reynolds numbers, both for unconfined circular and square cylinders (see, [10]).

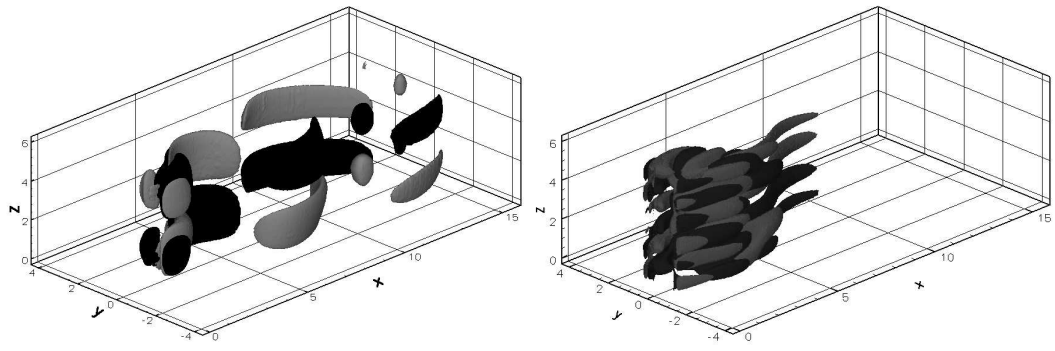

(a) (b)

Figure 5: (a) Streamwise vorticity in the wake obtained at $Re = 200$ and $t = 92.4$. The gray surface corresponds to $\omega_x = 0.1$, while the black one to $\omega_x = -0.1$. (b) Streamwise vorticity in the wake obtained at $Re = 300$ and $t \simeq 35$. The gray surface and black surfaces correspond to $\omega_x = 0.05$ and $\omega_x = -0.05$ respectively.

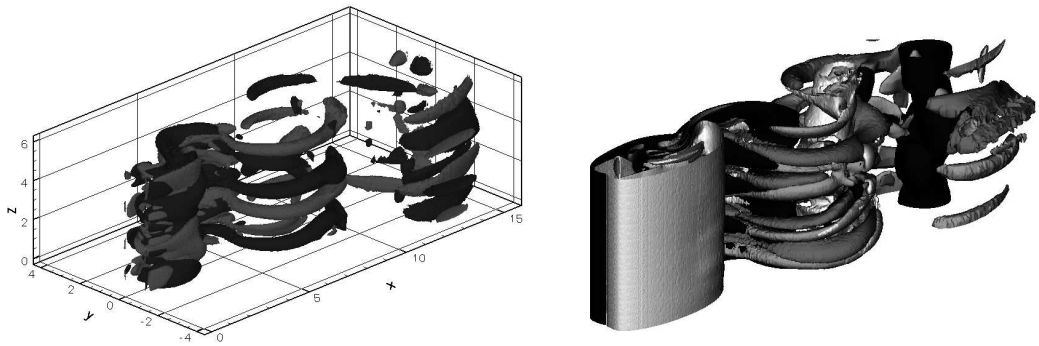

(a) (b)

Figure 6: (a) Streamwise vorticity in the wake obtained at $Re = 300$ and $t \simeq 57$. The gray surface identifies $\omega_x = 0.4$ and the black one $\omega_x = -0.4$. (b) Streamwise and spanwise vorticity components in the wake obtained at $Re = 300$ after the transient. The black and light gray surfaces correspond to $\omega_z = -0.4$ and $\omega_z = 0.4$ respectively. The streamwise tubes identify $\omega_x = 0.4$ and $\omega_x = -0.4$ respectively.

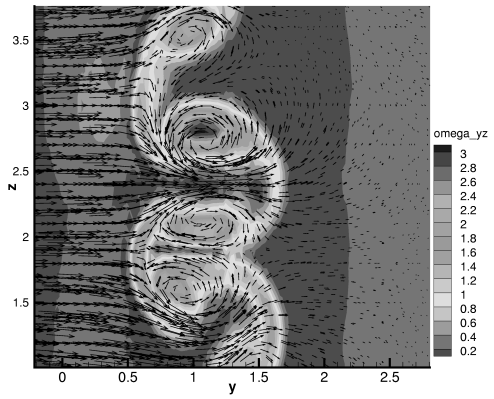

Figure 7: Velocity vectors in a (y, z) plane at $x = 4$ and modulus of the projection of the vorticity vector on the same plane; $Re = 300$ after the transient.

3 Low-order modeling

The possibility of reproducing a given dynamics is fundamental in devising even crudely approximated control laws by systematic means, e.g., optimal control theory. The main idea is to build a low-order model of an actuated flow from an existing database. Using this model, one computes the optimal actuation and applies it to the full approximation of the Navier-Stokes equations. If the error between this solution and that of the low-order model is not within a certain tolerance, then a new low-order model based on the latest Navier-Stokes solution is built. This iteration is performed until the error is within the tolerance. It was shown that the loop converges under certain assumptions ([1]). Clearly, the crucial ingredient of this approach is to be able to accurately reproduce the observed dynamics.

To this end, the discrete instantaneous velocity is expanded in terms of discrete empirical eigenmodes:

$$\boldsymbol{u}(\boldsymbol{x}, t) = \overline{\boldsymbol{u}}(\boldsymbol{x}) + \sum_{n=1}^{N_r} a_n(t)\boldsymbol{\phi}_n(\boldsymbol{x})$$

where $\overline{\boldsymbol{u}}(\boldsymbol{x})$ is a reference velocity field. The modes $\boldsymbol{\phi}_n(x)$ are found by proper orthogonal decomposition (POD) using the snapshots method of [16]. Only a limited number of modes (N_r) is used in the representation of velocity; in the spirit of the POD, they are the modes giving the main contribution to the flow energy.

The adopted numerical method discretizes the Navier-Stokes equations for compressible flows. However, the considered Mach number is low ($M = 0.1$) and the flow can be considered as incompressible since the density fluctuations are negligible. Hence, the construction of the POD modes

is based on the usual kinetic energy norm, and a Galerkin projection of the incompressible Navier-Stokes equations over the retained POD modes is carried out. As the POD modes are computed from the velocity fluctuations about the reference velocity field $\overline{\boldsymbol{u}}(\boldsymbol{x})$, the projection leads to the following low-order model:

$$\begin{aligned} \dot{a}_r(t) &= \left(C0'_r - B0_r + \frac{D0_r}{Re}\right) + \left(C1'_{kr} - B1_{kr} + \frac{D_{kr}}{Re}\right) a_k(t) - B_{ksr} a_k(t) a_s(t) \\ a_r(0) &= (\boldsymbol{u}(\boldsymbol{x},0) - \overline{\boldsymbol{u}}(\boldsymbol{x}), \boldsymbol{\phi}_r) \end{aligned} \tag{1}$$

where the Einstein summation convention is used, all the subscripts range from 1 to N_r and $(\cdot,\cdot)$ denotes the canonical L^2 inner product. The coefficients $B0_r$, $B1_{kr}$, B_{ksr}, $D0_r$ and D_{kr} derive directly from the Galerkin projection of the Navier-Stokes equations onto the POD modes and are defined by

$$\begin{aligned} B_{ksr} &= (\phi_k \cdot \nabla \phi_s \, , \phi_r) \\ D_{kr} &= (\Delta \phi_k \, , \phi_r) \\ B0_r &= (\overline{\boldsymbol{u}} \cdot \nabla \overline{\boldsymbol{u}} \, , \phi_r) \\ B1_{kr} &= (\overline{\boldsymbol{u}} \cdot \nabla \phi_k \, , \phi_r) + (\phi_k \cdot \nabla \overline{\boldsymbol{u}} \, , \phi_r) \\ D0_r &= (\Delta \overline{\boldsymbol{u}} \, , \phi_r) \end{aligned} \tag{2}$$

whereas the terms $C0'_r$ and $C1'_{kr}\, a_k(t)$ are added in order to model the interaction of the unresolved modes with the resolved ones. They also takes into account the effect of the pressure drop along the channel. By setting $C0_r = (C0'_r - B0_r + D0_r/Re)$ and $C1_{kr} = (C1'_{kr} - B1_{kr} + D_{kr}/Re)$, the system (1) reads

$$\begin{aligned} \dot{a}_r(t) &= C0_r + C1_{kr} a_k(t) - B_{ksr} a_k(t) a_s(t) \\ a_r(0) &= (\boldsymbol{u}(\boldsymbol{x},0) - \overline{\boldsymbol{u}}(\boldsymbol{x}), \boldsymbol{\phi}_r) \end{aligned} \tag{3}$$

At this point, the terms $C0_r$ and $C1_{kr}$ are *calibrated* using a pseudo-spectral method to take into account the pressure drop as well as the interaction of unresolved modes in the POD expansion. The calibration consists in solving an inverse problem where the coefficients $C0_r$ and $C1_{kr}$ are to be found such that the model prediction gets as close as possible in the L^2 norm to the actual reference solution. This problem is solved using an accurate and efficient optimisation method: accurate because the method is spectral, and efficient because the solution is obtained by solving a direct and an adjoint problem in one shot. See [5] for a detailed discussion.

In order to evaluate the possibility of modeling this flow by a reduced number of degrees of freedom, we consider two separate issues. As a first step, we a priori check if the flow admits a low dimensional representation. In other words, we study the approximation error of the flow snapshots as a function of the number of POD modes retained. Note that no dynamics is involved at this stage, it is merely a question of the POD modes actually spanning the solution manifold. The second issue concerns the error between the coefficients predicted by the calibrated model and the projection of the flow snapshots over the POD modes. This step is intended to verify if a quadratic model where the non-linear term is derived from the POD modes and the linear term is adjusted to fit the data, is capable of reproducing the dynamics of the flow.

POD case	Time interval	Number of snapshots
POD1	$382.24 < t < 397.61$	45
POD2	$360.23 < t < 412.64$	151
POD3	$94.38 < t < 412.64$	912
POD4	$5.3 < t < 59.45$	156

Table 3: POD database details.

With these objectives in mind, four different POD bases are computed using the flow snapshots obtained in the three-dimensional simulation at $Re = 300$. The first three proper orthogonal decompositions (POD1, POD2 and POD3) are pertinent to the developed flow, i.e., when the three-dimensional structures in the wake are clearly developed. The fourth one (POD4) is relative to the transient flow, i.e. when the three-dimensionality of the wake is developing. The details concerning the snapshot databases used are summarized in table 3. The time-averaged flow field was subtracted from each snapshot before carrying out the PODs for the developed flow, while the two-dimensional unstable steady solution was subtracted from each snapshot for the transient case.

The main motivation for using a different number of flow snapshots for the developed flow, is to show how the approximation properties of the POD modes depend on the flow database. To this end, we considered the reconstructed fluctuating energy for flow snapshots which are inside or outside the database used to determine the POD modes, figure 8 (a,b,c). The abrupt reduction of captured energy corresponds to snapshots which do not belong to the flow database. As the database becomes larger, this jump becomes smaller: it is seen that as the number of flow snapshots in the database increases, the energy captured using a given number of modes increases for the snapshots outside the database as expected, while it decreases for the snapshots inside the database. This is a consequence of the chaotic nature of the flow and of the larger snapshots space to be represented.

Moreover we see that taking a larger number of modes to build the model makes sense only for larger databases. Large numbers of flow snapshots need to be taken into account to recover high levels of fluctuating energy outside the database, even in this case where the Reynolds number is small compared to real applications. However, the dimensional reduction is from $O(10^7)$ degrees of freedom to $O(10^2)$ for case (c), recovering about 70% of fluctuating energy outside the database. For the transient (d) we see that 8 modes are enough to give a reasonable representation of energy.

Modes 1 and 3 relative to POD3 are shown in figure 9. The cylinder is not visualized, its axis being the intersection of the planes $x = 0$ and $y = 0$. The first mode is relative to the classical vortex alley, although some corrugations due to three-dimensional effects are visible in the x and y-components. The z-component is approximately one order of magnitude lower than the others, and it is at the threshold of numerical noise. The main time frequency of the coefficient associated to this mode is that of the vortex shedding. The third POD eigenfunction is of different nature as it presents structures elongated in the x-axis direction. Moreover, all its components have the same order of magnitude. This mode appears to be related to the evolution of the three-dimensional instability and to the interaction with the bounding walls. In time, the frequency of the corresponding Galerkin coefficient is much lower. The subsequent modes are of the same kind of the ones depicted.

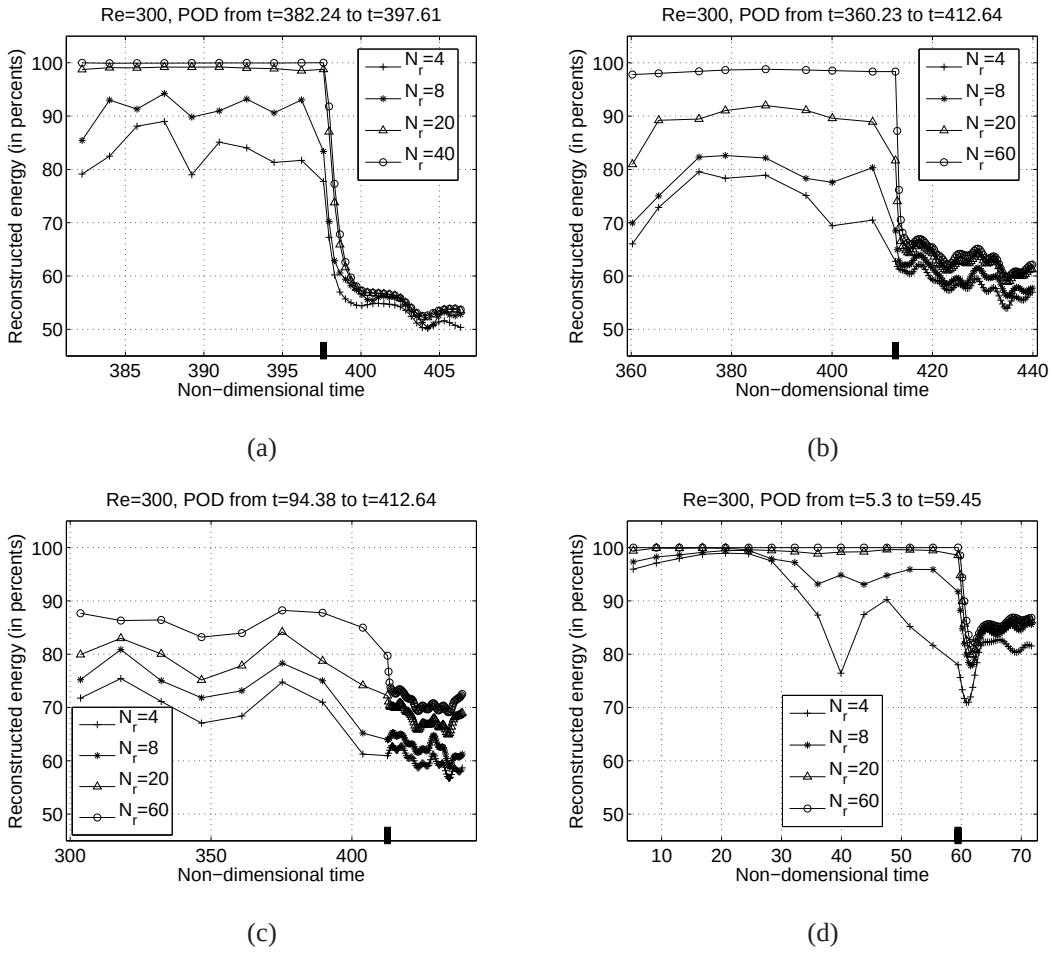

Figure 8: Percentage of reconstructed fluctuating energy for flow fields inside and outside the database. N_r is the number of modes. (a) POD1, (b) POD2, (c) POD3 and (d) POD4. The mark on the abscissa denotes the limit after which the reconstructed snapshots do not belong to the database.

They either represent smaller and smaller scales of the vortex shedding, or finer three-dimensional structures.

For POD2 and POD4, the resulting dynamical systems were calibrated over the corresponding databases of table 3, using 121 and 81 collocation points in POD2 and POD4 respectively. A comparison between the model and the reference simulation was carried out in terms of time-evolution of the POD modal coefficients and is shown in figure 11 and figure 10. The comparison was carried out for flow snapshots that are within the database used to compute the POD modes. Therefore,

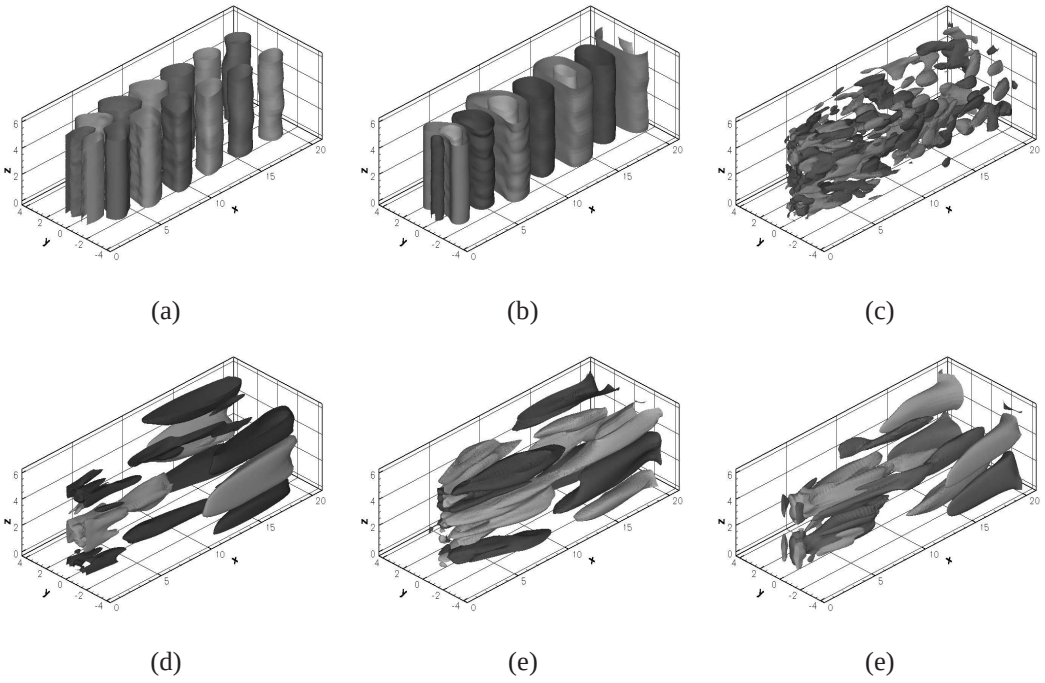

(a) (b) (c)

(d) (e) (e)

Figure 9: Components of the first (top) and third (bottom) mode relative to POD3. (a) x-component: light gray 0.015, dark gray -0.015; (b) y-component: light gray 0.05, gray 0.01, dark gray -0.04; (c) z-component: light gray 0.0035, dark gray = -0.0035; (d) x-component: light gray 0.032, dark gray -0.032; (e) y-component: light gray 0.02, dark gray -0.02; (f) z-component: light gray 0.025, dark gray -0.025.

figure 11 and figure 10 really show how the low-order model fits the solution database from which the POD modes were derived.

The physical phenomenon is far from being periodic. In the fully developed case we have low frequency modulations as well as high frequency bursts. In the transient case the spectrum is more compact but it is not steady. In both cases we are able to reproduce to a high level of accuracy the reference solution. As expected, the error is concentrated in the last modes, because the influence on these scales of the unresolved dynamics is higher. Since the simulation of the low-order dynamical system matches with good accuracy the reference results, it follows that the the error in the physical space is of the order of the approximation error seen in figure 8.

An additional model was computed for POD1. Also in this case the predictions are accurate compared to the reference solution. The model coefficients depend on the calibration database in a non-trivial way since they result in part from an inverse problem. However, it can be observed that in both POD1 and POD2 the matrix C_{kr} shows a couple of complex conjugate eigenvalues

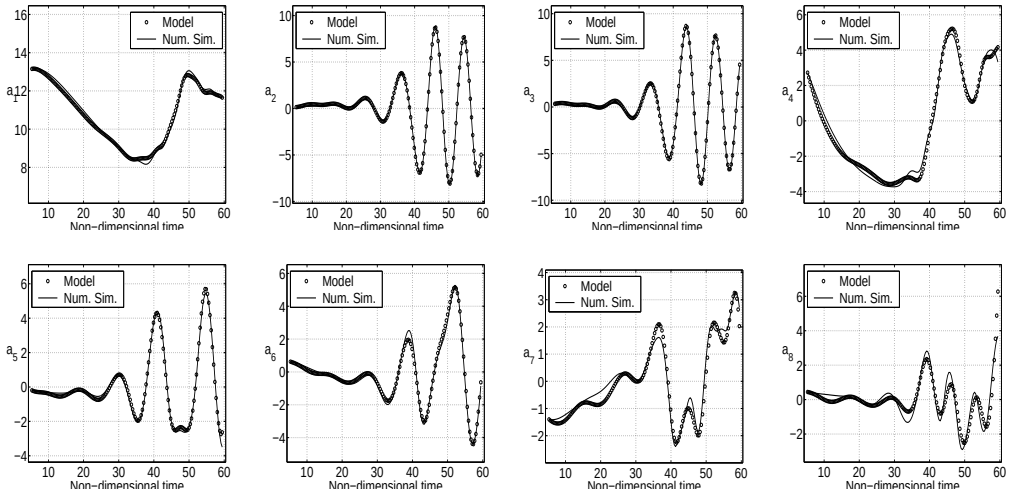

Figure 10: Transient after the impulsive start-up: projection of the fully resolved Navier-Stokes simulations over the POD modes (continuous line) vs. the integration of the dynamical system obtained retaining the first 8 POD modes (circles).

whose imaginary part is nearly equal to the frequency of the vortex shedding. The corresponding eigenvectors are mainly in the direction of the first and second POD mode. This feature was also observed in [5] for the two-dimensional instability leading to vortex shedding.

Finally, in the derivation of the reduced models, we are presently limited by the number of POD modes retained and the number of collocation points used to calibrate the flow (see [5] for details) because of the non-linear optimization problem size: in the case of POD2 we solve an optimization problem with 5260 controls.

4 Concluding remarks

Accurate "plant models" of flows whose dynamics are characterized by complex large scale structures can be derived from simulation data sets. Within the range of calibration, the error between the flow predicted by such models and the reference solution is bounded. Moreover, it is of the order of the approximation error of the original data set projected over the POD modes, thanks to the pseudo-spectral approach employed. One result is hence that the adaptive control method proposed in [1] could be applied in this case over time horizons of the order of 10 shedding cycles. However, the possibility of using calibrated POD models as a predictive tool seems to be very remote in cases like the present where the spatial and temporal complexity is important. Indeed, the reconstruction error becomes relevant as soon as we take flow solutions that lie outside the snapshot range. Using $O(10^3)$ snapshots and 60 POD modes, the representation error is still of the order of 30% of the fluctuating

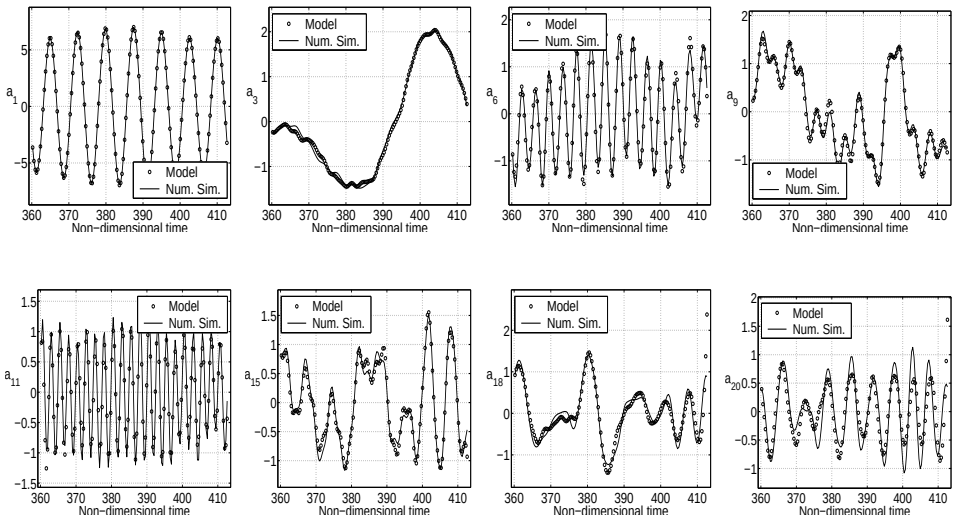

Figure 11: Developed three-dimensional flow: projection of the fully resolved Navier-Stokes simulations over the POD modes (continuous line) vs. the integration of the dynamical system obtained retaining the first 20 POD modes (circles). Only 8 representative modal coefficients are shown here.

energy. For this reason there will be an exponential divergence between any model prediction and the actual solution outside the snapshot range. Nonetheless one aspect is important: if the objective is to recover an estimate of the flow field from boundary measurements, as it will be shown in the next chapter, then such an error might still be acceptable.

In conclusion, the relevance of POD models based on the calibration procedure is that they can be used to determine control laws instead of the full Navier-Stokes equations, when the model includes the effect of the actuators. We mention that the grids used, their size as well as the number of flow snapshots can be representative of engineering problems, as a step to application of low-order models to practical flows.

Acknowledgements

This work was funded in part under the HPC-EUROPA project (RII3-CT-2003-506079). We thank M. Breuer for sharing his results with us, B.R. Noack, L. Cordier and C-H. Bruneau for useful discussions, A. Dervieux and B. Koobus for making available the core of the Navier-Stokes solver. IDRIS (Orsay, France), CINECA (Bologna, Italy) and M3PEC (Université Bordeaux 1, France) provided the computational resources. We are thankful to the “cellule informatique” at the Institut de Mathématiques de Bordeaux - in particular to P. Depouilly and S. Layrisse for their help with the data management.

References

[1] M. Bergmann, L. Cordier, and J.-P.Brancher. Optimal rotary control of the cylinder wake using proper orthogonal decomposition reduced-order model. *Physics of Fluids*, 17:097101, 2005.

[2] M. Breuer, J. Bernsdorf, T. Zeiser, and F. Durst. Accurate computations of the laminar flow past a square cylinder based on two different methods: lattice-Boltzmann and finite-volume. *International Journal Heat and Fluid Flow*, 21:186–196, 2000.

[3] S. Camarri and F. Giannetti. On the inversion of the Kármán street in the wake of a confined square cylinder. 2006. Submitted to *J. Fluid Mech.*

[4] S. Camarri, M. V. Salvetti, B. Koobus, and A. Dervieux. A low-diffusion MUSCL scheme for LES on unstructured grids. *Computers and Fluids*, 33:1101–1129, 2004.

[5] B. Galletti, A. Bottaro, CH. Bruneau, and A. Iollo. Accurate model reduction of transient flows. Technical Report RR-5676. `http://www.inria.fr/rrrt/rr-5676.html`, INRIA, 2005.

[6] B. Galletti, C. H. Bruneau, L. Zannetti, and A. Iollo. Low-order modelling of laminar flow regimes past a confined square cylinder. *J. Fluid Mech.*, 503:161–170, 2004.

[7] W. R. Graham, J. Peraire, and K. Y. Tang. Optimal control of vortex shedding using low-order models. part i. *International Journal for Numerical Methods in Engineering*, 44:945–972, 1998.

[8] H. Guillard and C. Viozat. On the behaviour of upwind schemes in the low mach number limit. *Computers and Fluids*, 28:63–86, 1999.

[9] J. L. Lumley. The structure of inhomogeneous turbulent flows. In *Atmospheric Turbulence and Radio Wave Propagation*, edited by A. M. Yaglom and V. L. Tatarski. Nakua, Moscow., pages 166–178, 1967.

[10] SC. Luo, YT. Chew, and YT Ng. Characteristics of square cylinder wake transition flows. *Phys. Fluids*, 15(9):2549–2559, 2003.

[11] X. Ma and G. E. Karniadakis. A low-dimensional model for simulating three-dimensional cylinder flow. *Journal of Fluid Mechanics*, 458:181–190, 2002.

[12] R. Martin and H. Guillard. A second order defect correction scheme for unsteady problems. *Computers and Fluids*, 25(1):9–27, 1996.

[13] J. Robichaux, S. Balachandar, and S P. Vanka. Three-dimensional Floquet instability of the wake of square cylinder. *Phys. Fluids*, 11(3):560–578, 1999.

[14] PL. Roe. Approximate riemann solvers, parameters vectors, and difference schemes. *J. Comp. Physics*, 43:357–372, 1981.

[15] A. K. Saha, G. Biswas, and K. Muralidhar. Three-dimensional study of flow past a square cylinder at low reynolds number. *International Journal of Heat and Fluid Flow*, 24:54–66, 2003.

[16] L. Sirovich. Turbulence and the dynamics of coherent structures. Parts I,II and III. *Quarterly of Applied Mathematics*, XLV:561–590, 1987.

[17] A. Sohankar, C. Norberg, and L. Davidson. Simulation of three-dimensional flow around a square cylinder at moderate reynolds numbers. *Physics of Fluids*, 11(2):288–306, 1999.

[18] H. Telib, M. Manhart, and A. Iollo. Analysis and low-order modeling of the inhomogeneous transitional flow inside a T-mixer. *Phisics of Fluids*, 8:2717–2731, 2004.

[19] B. van Leer. Towards the ultimate conservative scheme. iv: A new approach to numerical convection. *J. Comp. Physics*, 23:276–299, 1977.

[20] L. Zovatto and G. Pedrizzetti. Flow about a circular cylinder between parallel walls. *J. Fluid Mech.*, 440:1–25, 2001.

Unité de recherche INRIA Futurs
Parc Club Orsay Université - ZAC des Vignes
4, rue Jacques Monod - 91893 ORSAY Cedex (France)

Unité de recherche INRIA Lorraine : LORIA, Technopôle de Nancy-Brabois - Campus scientifique
615, rue du Jardin Botanique - BP 101 - 54602 Villers-lès-Nancy Cedex (France)
Unité de recherche INRIA Rennes : IRISA, Campus universitaire de Beaulieu - 35042 Rennes Cedex (France)
Unité de recherche INRIA Rhône-Alpes : 655, avenue de l'Europe - 38334 Montbonnot Saint-Ismier (France)
Unité de recherche INRIA Rocquencourt : Domaine de Voluceau - Rocquencourt - BP 105 - 78153 Le Chesnay Cedex (France)
Unité de recherche INRIA Sophia Antipolis : 2004, route des Lucioles - BP 93 - 06902 Sophia Antipolis Cedex (France)

Éditeur
INRIA - Domaine de Voluceau - Rocquencourt, BP 105 - 78153 Le Chesnay Cedex (France)
http://www.inria.fr
ISSN 0249-6399